Full Paper

Journal of the Brazilian Chemical Society

https://dx.doi.org/10.21577/0103-5053.20250108

J. Braz. Chem. Soc. **2025**, *36*, 11, e-20250108, 1-15

Leishmania chagasi Dihydrofolate Reductase-Thymidylate Synthase Potential Inhibitors Identified by Virtual Screening

Luíza M. de Macêdo,[a] Quezia V. F. S. da Fonseca,[a] Iris C. dos Santos,[a] Quézia L. S. Sampaio,[b] Janine F. S. Silva,[b] Moyses F. de Araujo Neto,[b] Aníbal F. Santos Júnior,[b]*,[a] Erika M. O. Ribeiro,[a] Franco H. A. Leite,[b] Humberto F. de Freitas,[b] Samuel S. R. Pita[c] and André L. B. Teles[a]*,[a]

[a]*Laboratório de Modelagem Molecular, Departamento de Saúde, Universidade do Estado da Bahia (UNEB), R. Silveira Martins, 2555, Cabula, 41150-000 Salvador-BA, Brazil*

[b]*Laboratório de Química Informática e Avaliação Biológica (LaqBio), Departamento de Saúde, Universidade Estadual de Feira de Santana (UEFS), Av. Transnordestina, Novo Horizonte, 44036-900 Feira de Santana-BA, Brazil*

[c]*Laboratório de Bioinformática e Modelagem Molecular (LaBiMM), Faculdade de Farmácia, Universidade Federal da Bahia (UFBA), Av. Barão de Jeremoabo, 147, Ondina, 40170-115 Salvador-BA, Brazil*

Visceral leishmaniasis is a disease with high lethality indicators and considerable incidence in Latin America, Africa, and Asia. Given the need to develop new drugs to treat leishmaniasis, this study aimed to identify potential selective compounds against *Leishmania chagasi* dihydrofolate reductase-thymidylate synthase (*Lc*DHFR-TS). The SYBYL®-X 2.0 program was used to generate the pharmacophoric hypotheses of the dihydrofolate reductase (DHFR) from *Homo sapiens* and *L. chagasi* (Pareto = 0; Receiver Operating Character (ROC)/area under the curve (AUC) > 0.75). Molecules from the banks of Sigma-Aldrich® and Medicines for Malaria Venture (MMV) were screened by pharmacophoric models; 254 compounds showed stereo-electronic requirements only against *Lc*DHFR, and these molecules were submitted to physical-chemical, toxicological, and commercially available filters. The resulting 24 were submitted to docking on the GOLD 5.3 program; for such, the MODELLER 9.18 program was used to build a homology model of *Lc*DHFR-TS. The two best scores were submitted to the Molecular Dynamics (MD) simulations of 110 ns on the Gromacs program. It was found that SUB10 and SUB22 perform hydrogen interactions with residues Lys82 and Asp-52, respectively, for periods longer than 50%. These compounds have commercial availability and should, therefore, be prioritized for subsequent steps in planning new drug candidates.

Keywords: anti-leishmania, dihydrofolate reductase thymidylate synthase, pharmacophore model, molecular docking, molecular dynamics

Introduction

Neglected diseases (ND) groups 20 diseases represented by dengue, schistosomiasis, leprosy, leishmaniasis, and malaria that predominantly affect tropical regions, inflicting severe social, economic, and health consequences on over one billion individuals worldwide.[1] Despite this scenario, the pharmaceutical industry exhibits little interest in developing novel drugs for them due to their reduced profitability.[2]

Among the neglected diseases, leishmaniasis, caused by protozoa of the *Leishmania* genus, stands out as one of the six most important endemic diseases of the world. This disease is prevalent in 102 countries worldwide, with higher occurrence in tropical and subtropical regions, accounting for 220,315 new cases reported in 2020.[1-4] About 1 billion individuals live in areas with a high risk of leishmania infections.[1-5] In Brazil, there were 18,365 diagnosed cases and 236 deaths related to the disease in 2020.[6-8]

Leishmaniasis manifests in four distinct clinical forms: Cutaneous Leishmaniasis (CL), Mucocutaneous Leishmaniasis (MCL), Diffuse Cutaneous Leishmaniasis (DCL), and Visceral Leishmaniasis (VL).[9]

*e-mail: afjunior@uneb.br; alteles@uneb.br
Editor handled this article: Paulo Augusto Netz (Associate)

Among these forms, VL is the most severe disease and life-threatening, with a fatality rate of up to 90%.[7,8] The etiological agents of VL are *Leishmania chagasi*, *Leishmania donovani*, and *Leishmania major*, which are transmitted through blood meal by sandflies belonging to the *Lutzomyia* genus.[9,10] Globally, VL accounts for 12,838 reported cases in 2020, with 3,813 deaths recorded between 2014 and 2020. Notably, 95% of these deaths were concentrated in 10 countries: Brazil, Ethiopia, India, Kenya, Paraguay, Bangladesh, Nepal, Somalia, Sudan, and South Sudan.[1,7] In Brazil, where *L. chagasi* is the main etiological agent of VL, with 1,933 reported cases in 2020 resulting in 162 deaths.[7,8]

Clinical manifestations of VL are prolonged fever, anemia, splenomegaly, hepatomegaly, weight loss, cutaneous-mucosal pallor, and diarrhea,[9,11] and their treatment involves pentavalent antimonials, pentamidines, and amphotericin B.[12,13] However, the pharmacology treatment for VL is severely limited by bioavailability and tolerance issues such as parenteral administration and adverse reactions such as cardiotoxicity and hepatotoxicity.[6,12,13] These limitations contribute to low adherence and reinforce the need for new therapeutic alternatives.

The search for compounds that selectively inhibit essential therapeutic targets involved in the biological hassle of the parasite has been employed to achieve this goal.[14] In this regard, the pharmacological targets associated with the folate metabolic pathway in *L. chagasi* are particularly noteworthy, as their inhibition hinders the formation of essential vital metabolites required for deoxyribonucleic acid (DNA) and ribonucleic acid (RNA) synthesis, ultimately leading to parasite death. Among the targets within this pathway, dihydrofolate reductase (DHRF; E.C. 1.5.1.3) stands out as a promising target for developing new drugs. DHFR is a crucial enzyme in converting dihydrofolate (DHF) into tetrahydrofolate (THF), an essential parasite's metabolite of thymidine synthesis employed in DNA synthesis.[15-17] Furthermore, Vickers and Beverley[18] demonstrated that silencing the DHFR gene reduced the viability of the parasite inside infected cells by *Leishmania* protozoa, thus hindering the infection. Moreover, in *Leishmania* and other protozoans, DHFR is fused to thymidylate synthase (TS),[16] giving a DHFR-TS complex, which is essential to deoxythymidine monophosphate (dTMP) production and DHF regeneration.[19]

Additionally, there are evolutionary differences in the DHFR gene sequences across several organisms, which provides an opportunity to develop selective inhibitors to *Leishmania* DHFR-TS, mainly *L. chagasi's* DHFR-TS (*Lc*DHFR-TS), while sparing the enzyme of the host to minimize adverse reactions in patients undergoing treatment.[18]

Therefore, *L. chagasi* DHFR-TS is a promising target for designing new drugs against VL, and many *in silico* strategies have been successfully used in drug discovery projects. They could be applied to find selective inhibitors against *Lc*DHFR-TS.[20-22] This study applied some computational chemistry approaches (homology and pharmacophoric modeling, molecular docking, and molecular dynamics) to identify potential selective inhibitors of *Lc*DHFR-TS, contributing to designing new therapeutic alternatives against VL.

Methodology

The flowchart (Figure 1) summarizes the methodological steps of this work. The virtual screening process involved three steps. Firstly, pharmacophoric models were designed to identify potential inhibitors of *Lc*DHFR-TS and *Homo sapiens* DHFR (*Hs*DHFR). Molecules from commercial and free compound databases were screened, targeting *Lc*DHFR-TS and *Hs*DHFR. Physicochemical, toxicological, and commercial availability filters were then carried out over the compounds with the potential

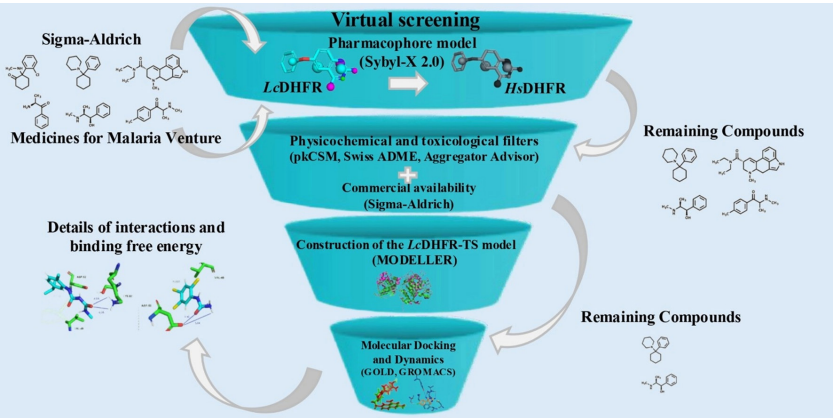

Figure 1. Flowchart summarizing the steps taken to perform virtual screening and identify potential selective inhibitors of *Lc*DHFR-TS.

for selective inhibition of *Lc*DHFR-TS (those that fit the *Lc*DHFR-TS model but not the *Hs*DHFR model). Homology modeling of the parasite target protein structure was carried out, which allowed the investigation of the interactions and binding free energy between compounds from previous steps and *Lc*DHFRT-TS through docking and molecular dynamics simulations.

Dataset

A dataset of 14 *L. donovani* DHFR (E.C. 1.5.1.3) and *L. chagasi* DHFR (E.C. 1.5.1.3) inhibitors with experimental data (selectivity index (SI) ≥ 3 fold),[20-26] was employed to training and test set in pharmacophore model generation and validation step (Table S1, Supplementary Information section). In addition, ten *Homo sapiens* DHFR (*Hs*DHFR) (E.C. 1.5.1.3) inhibitors were employed to create a pharmacophoric model explicitly targeting the human enzyme[27] (Table S1). The test set of *Hs*DHFR inhibitors was acquired from the DUD-E server.[28]

Marvin Sketch 16.9.5 program[29] was employed to select the most reliable tautomers of all compounds collected in the previous steps. Subsequently, the CONCORD module of SYBYL®-X 2.0[30] was used to generate the 3D structures of the inhibitors, considering the protonation profile at pH = 7.0.[20] The optimization of the 3D structures of the inhibitors was performed using the Conjugate Gradient (GC) method with a convergence criterion of 0.001 cal mol^{-1}, employing the Tripos force field ($\varepsilon = 80.4$) and setting a maximum of 50.000 interactions.[31] Furthermore, Gasteiger Huckel charges[32] were assigned to the compounds on the SYBYL®-X 2.0 platform.[30]

Pharmacophore model construction

As available in the SYBYL®-X 2.0 package,[30] the Galahad module generated the *L. chagasi* and *H. sapiens* pharmacophore models. Each training dataset was flexibly aligned to build hypermolecular alignments that map standard pharmacophore features. The genetic algorithm employed in this step starts with a maximum of 40 generations (population size) of each *Lc*DHFR inhibitor and 50 to *Hs*DHFR inhibitor. The generic operators (mutation rate, mutation decay, and crossover rate) were set to 1.0 during the modeling process.

Pharmacophore model evaluation

The *Lc*DHFR and *Hs*DHFR pharmacophore models were evaluated by their ability to differentiate true inhibitors from decoys. The decoys were obtained from the DUD-E server[28] at the rate of 50 decoys for each active compound. The areas under the Receiver Operating Character (ROCs)[33] were calculated to assess the specificity and sensitivity of each model. Only models with area under the curve (AUC) ≥ 0.70 were considered. Pharmacophore models with AUC > 0.7 were evaluated by their ability to recover more active compounds among the top 2% of ranked compounds by the enrichment factor calculation (equation 1).[34]

$$EF\,(x\%) = \frac{\dfrac{n\,(\text{No. of actives in x\% of the database})}{n\,(\text{total No. of compounds in x\% of the database})}}{\dfrac{n\,(\text{No. of actives present in the database})}{n\,(\text{total No. of compounds in the database})}} \quad (1)$$

In this equation, "x%" represents the percentage of the database considered, and the enrichment factor (EF) indicates how much the active compounds are enriched in that portion of the database compared to the overall database. A higher EF value indicates a better enrichment of active compounds in the selected subset of the database.

Pharmacophore-based virtual screening

The best *Lc*DHFR and *Hs*DHFR pharmacophore models were employed to screen the Sigma-Aldrich® catalog[35] and the Medicines for Malaria Venture molecule bank.[36] The pharmacophore models were converted into a 3D search using the UNITY module of SYBYL®-X 2.0,[30] and the compounds from catalogs were ranked according to their QFIT values (or Quality Fit, a numerical score, 0-100, that indicates how well a molecule aligns with a pharmacophore model, with higher values representing better fits). Compounds with a QFIT value > 0 for the human enzyme model were discarded. For the remaining molecules, those with QFIT values higher than the mean plus two times the standard deviation of the QFIT values of all remaining compounds were prioritized (equation 2).

$$X = a + 2\sigma \quad (2)$$

where X is the cut-off QFIT value, a is the average of the QFIT values of the screened bank, and σ is the standard deviation.

Applying this criterion, the compounds that exhibited QFIT values above the cut-off point were considered potential hits for further evaluation as potential compounds with stereo-electronic features only for *Lc*DHFR.

Physico-chemical, toxicological filters and commercial availability evaluation

The compounds prioritized in pharmacophore-based

virtual screening were evaluated using the SwissADME server for oral bioavailability.[37] Compounds with positive prediction of this parameter (number of hydrogen bond acceptors (≤ 10), hydrogen bond donor groups (≤ 5), molecular mass (≤ 500), octanol-water partition coefficient (cLogP) (≤ 5) and topological area of polar surface TPSA)[38,39] were then submitted to ProTox 3.0[40] and pkCSM[41] servers, to predict toxicity (acute toxicity, cardiotoxicity, hepatotoxicity and mutagenicity), and Aggregator Advisor,[42] to evaluate aggregation profiles. Compounds without penalties regarding these parameters and commercially available were prioritized for subsequent steps.

*Lc*DHFR-TS 3D prediction model

The primary sequence of *Lc*DHFR-TS (Genbank code: NC_009277) was aligned to the 3D structures of *Trypanosoma cruzi* (PDB: 3KJS) and *Trypanosoma brucei* (PDB: 3QFX) DHFR-TS using the Clustal Omega server.[43] The MODELLER 9.18,[44] was then used to build 100 three-dimensional *Lc*DHFR-TS:DHF: NADPH complex models. These models were ranked according to the value of Qualitative Model Energy Analysis (QMEAN).[45]

Subsequently, the ten best models were evaluated for stereochemical quality using SAVES v. 6.0.[46] Additionally, the compatibility between the primary sequence and the three-dimensional unfolding of the models was assessed using the VERIFY 3D server.[47] The *Lc*DHFR-TS:DHF: NADPH complex model (NADPH refers to the DHFR cofactor, whose acronym stands for nicotinamide adenine dinucleotide phosphate), whose *Lc*DHFR-TS coordinates were used in the docking and molecular dynamics studies, was obtained through homology modeling.

Docking based-virtual screening

The compounds prioritized in prior steps were employed on molecular docking by GOLD 5.3 software.[48] Before docking calculation, the 3D structures of the compounds were generated using the CONCORD module of SYBYL®-X 2.0,[30] following the same settings in the dataset topic.

For the enzyme structure, the biopolymer module of SYBYL®-X 2.0,[30] was used to remove water molecules, ions, and artifacts, and hydrogens were added in standard geometry. The protonation states of residues in the catalytic region were defined using the H++ server,[49] considering a pH of 7.0.[20] The docking calculations were focused on the catalytic site of *Lc*DHFR-TS, with coordinates based on the position of the DHF present in the model built in the previous step.

Before the calculations, the scoring functions (ASP, Goldscore, ChemPLP, and Chemscore) of the GOLD 5.3 software[48] were evaluated for the ability to reproduce the substrate pose (DHF) as well as the capability to discriminate between true inhibitors and decoys available on the DUD-E platform.[28] The discrimination data were assessed using AUC values from the ROC curve.[33] Likewise, equation 1 was also used to identify the best scoring function used in virtual screening by molecular docking.[50,51]

The 3D structures of the compounds obtained from the pharmacophore screening and other filters were then submitted to the molecular docking routine using the ASP scoring function rescored with the GoldScore function. This step allowed the flexible search for the most stable interaction pose of each compound against *Lc*DFHR-TS and the ordering of the compounds based on the affinity score for the enzyme.

Molecular dynamics simulation

MD simulations were carried out with the GROMACS 2021.3 software[52-59] for different *Lc*DHFR-TS systems in apo; in complexes with NADPH, pyrimethamine (PYR), substance 10 (SUB10), and substance 22 (SUB22). The topologies of the ligands were generated in the ATB 3.0 server.[60]

The starting coordinates for the ligands were obtained from the docking pose, except for pyrimethamine, which was obtained from the *T. brucei* DHFR-TS complex (PDB ID: 3QFX) through the structural overlap of *T. brucei* and *L. chagasi* enzymes,[61] and NADPH, obtained from the *Lc*DHFR-TS:DHF: NADPH model built by homology modeling.

Each system was initially minimized using the steepest descent algorithm until the forces were less than 10 kJ mol^{-1} nm^{-1}. A second minimization step was performed using the conjugate gradient method. Following this, one nanosecond (ns) simulation was conducted with restriction on the position of non-hydrogen atoms (pre-equilibrium stage), assuming NPT ensemble conditions.

After these steps, the simulations without restrictions were performed with the following parameters: time = 200 ns, 1 atm, 310 K, pH 7.0, GROMOS54A7 force field,[62] electrostatic treatment (PME)[62] with a cut-off radius of 1.0 nm for non-covalent interactions, periodic boundary conditions (PBC), write rate of 2 ps, SPC/E water model,[54] box of dodecahedral simulation. Na^+ and Cl^- were added to the system at a concentration of 150 nM to ensure isotonicity. Basic residues (Arg, Lys) and acid residues (Asp, Glu) were deprotonated to mimic the biological condition, except for Glu176 and Glu292.

Histidine residues were handled following the microspecies according to the best interactions within the *Lc*DHFR-TS.

Molecular dynamics analysis

The system stabilities were performed using the root mean square deviation (RMSD) through the g_rms module in the GROMACS 2021.3 software.[52-57] Additionally, the radius of gyration and secondary structure were also evaluated by g_gyrate and do_dssp GROMACS tools. Hydrogen bond analysis was performed in the H-bond module and the HbMap2Grace[58] program. The molecular surface area analysis was also calculated using the SurfinMD[59] Program.

Results and Discussion

Pharmacophore models

Definition of training and test sets

Virtual screening by pharmacophoric models represents a pivotal strategy with the potential to accelerate drug discovery. Several studies have demonstrated its efficacy in identifying bioactive compounds, thus validating its application as a tool for the drug candidate design.[50,63]

In the context of drug design against leishmaniasis, considering the desirable safety profile for a drug against this pathology is of utmost importance, given the severe limitations of the current therapeutic options.[12,13] Therefore, caution is required to increase the likelihood of prioritizing selective compounds, as the DHFR domains of the *L. chagasi* and *H. sapiens* enzymes exhibit a sequential identity of 30% and conserve the scaffold between them.[16] To address this concern and avoid prioritizing compounds with off-target undesirable activity thus, a pharmacophoric model for DHFR from *H. sapiens* was also built and used to identify potential inhibitors of this human enzyme.

The success of the employed computational strategies is directly linked to the survey of DHFR inhibitors of *L. chagasi* and *H. sapiens* described in the literature.[63] Hence, selecting compounds based on potency and chemical diversity is essential in pharmacophoric models to identify the stereo-electronic requirements to inhibit the target enzyme and preserve the structural diversity of potentially active compounds. Based on this assumption, the selection of chemical structures to compose the model prioritized structural diversity (Table S1).[15]

Success in prioritizing potential inhibitors based on the pharmacophoric pattern of compounds with already known activity is also related to the quality of the generated pharmacophoric models.[64-66] In this context, the goal of selecting potent inhibitors with structural diversity and capable of binding to *Lc*DHFR-TS can be a challenge for the construction of pharmacophoric models.

Construction and evaluation of *Lc*DHFR and *Hs*DHFR pharmacophore models

The overlapping of chemical structures to identify pharmacophore patterns may encounter limitations when aligning molecules with different chemotypes and conformational arrangements, leading to models with energetic penalties.[64-66] Flexible alignment methods, such as genetic algorithms, have been employed to align compounds with chemical diversity to overcome this challenge.

In this work, the GALAHAD™ was employed to generate a hipermolecular hypothesis by offering the advantage of defining the lowest energy conformers and flexibly aligning them using the genetic algorithm.[67,68] According to the genetic algorithm heuristic, ten pharmacophore models were generated for *Lc*DHFR-TS and *Hs*DHFR (Table 1).

Among 10 pharmacophore models generated for each organism, four models of *Lc*DHFR-TS and one of *Hs*DHFR were discarded based on strain energy criteria (< 100.0 cal mol^{-1}).[68] The remaining models were evaluated based on the Pareto index, which normalizes the Mol_qry, H_bond, and Sterics parameters. The analysis revealed that all models were statistically equivalent regarding such parameters (Table 1). Thus, a widely used strategy was applied to assess the capability of the model to distinguish active compounds from false positives (decoys), aiming to resolve this stalemate. The evaluation comprises calculating the area under the ROC curve (Figure 2) to determine the specificity and selectivity of the models.[50,69,70]

An ideal curve would have an area under the curve (AUC) equal to 1.0, meaning the model identifies all active compounds before the decoys. Models with AUC > 0.70 are considered moderately predictive, AUC above 0.80 are considered good, and AUC values between 0.9 and 1.0 are considered excellent.[50,69,70]

Among the pharmacophore models generated for *Lc*DHFR-TS, model 10 showed the highest AUC value (AUC = 0.90) (Figure 2a) and the best enrichment rate among the top 2% ranked compounds, according to equation 1 (Table 2). Therefore, model 10 was selected for virtual screening. Similarly, for *Hs*DHFR, model 3 was chosen due to its superior AUC and recovery rate of active compounds in the database's initial phases (Figures 2a and 2b).

The best *Lc*DHFR-TS pharmacophore model consists of three hydrophobic centers (HY), three hydrogen interaction donor points (HBD), and one hydrogen

Table 1. GALAHAD internal statistical consistency data of pharmacophoric models generated for dihydrofolate reductase from *L. chagasi* (*Lc*DHFR-TS) and *Homo sapiens* (*Hs*DHFR)

Model ID	*Lc*DHFR-TS					*Hs*DHFR				
	Pareto	Energy / (cal mol^{-1})	Sterics	H bond	Mol_qry	Pareto	Energy / (cal mol^{-1})	Sterics	H bond	Mol_qry
01	0	27.71	110.30	51.30	21.86	0	18.66	214.80	95.80	43.46
02	0	15701.00	121.20	54.60	15.77	0	12.44	198.10	97.20	29.57
03	0	19210.40	122.40	53.50	21.29	0	18.58	195.10	96.70	37.75
04	0	14.16	90.10	49.60	16.80	0	14.95	204.20	94.50	34.13
05	0	36.01	144.80	44.60	11.47	0	15.99	201.30	95.50	56.35
06	0	118.18	121.40	49.90	14.13	0	26.61	211.00	98.30	27.08
07	0	161.16	126.70	48.30	16.32	0	10.17	191.40	94.70	32.34
08	0	69.64	143.20	49.90	8.95	0	5747116.50	205.70	103.90	30.05
09	0	15.77	104.50	48.80	14.23	0	11.28	203.00	96.50	29.90
10	0	21.79	106.90	51.50	10.73	0	9.83	204.20	91.80	41.49

interaction acceptor point (HBA). These convergent points are similar to the model elaborated against DHFR of *Mycobacterium tuberculosis*,[71] highlighting three hydrophobic sites and hydrogen bond donors as essential for ligand recognition. In addition, a model created against *T. cruzi*,[72] presented four hydrophobic centers, two hydrogen bond donor points, and one ionizable point, further supporting the findings of our study, which proposes at least three hydrophobic centers and two hydrogen bond donors as crucial for inhibiting trypanosomatids DHFR.

The selected model for *Hs*DHFR comprises three hydrophobic centers, four hydrogen bond donor points, and four hydrogen bond acceptors. This model closely aligns with the proposal of Arooj *et al.*,[73] which suggests a model with two hydrophobic centers, two hydrogen bond donors, and six hydrogen bond acceptors. It also shares similarities with the model developed by Rana *et al.*,[74] which includes one hydrophobic center, four hydrogen interaction donor points, and two hydrogen interaction acceptor points. The studies suggest that, unlike the *Lc*DHFR-TS model, hydrogen interaction acceptor points are among the essential characteristics for activity against the human enzyme. These findings indicate that the differences between the models may favor the identification of potentially parasite-selective compounds.

The superimposition of two inhibitors with different potencies on *Lc*DHFR-TS model No. 10 (Figure S1, Supplementary Information section) illustrates the ability of the model to adjust the structural features present in different inhibitors. This observation further validates the sensitivity of the model in accurately representing the ligand-binding interactions.

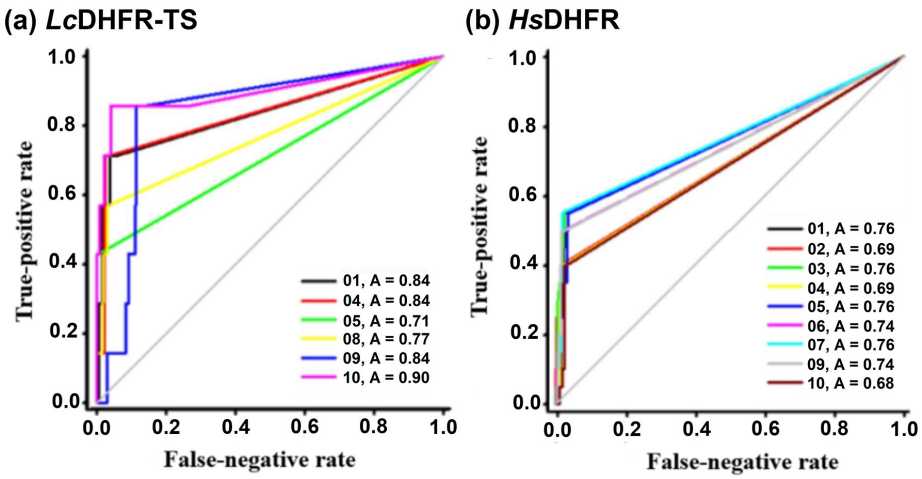

Figure 2. Receiver Operating Character (ROC) curve of *L. chagasi* dihydrofolate reductase thymidylate synthase (*Lc*DHFR-TS) and *H. sapiens* dihydrofolate reductase (*Hs*DHFR) models. Receiver Operating Character curves and area under the curve (AUC) values of *Lc*DHFR-TS (a); and *Hs*DHFR (b); models aligned with a database with inhibitors and decoys (1:50).

Table 2. Enrichment rates of active compounds recovered at the 2% best-ranked compounds in the database employed on the evaluation of *Lc*DHFR-TS and *Hs*DHFR pharmacophore models

*Lc*DHFR-TS		*Hs*DHFR	
Model ID	Actives recovered in the first 2% of all compounds sorted by qfit / %	Model ID	Actives recovered in the first 2% of all compounds sorted by qfit / %
01	43	01	30
04	14	03	35
05	43	05	25
08	29	06	20
09	0	07	30
10	57	09	20

*Lc*DHFR-TS: *Leishmania chagasi* dihydrofolate reductase-thymidylate synthase; HsDHFR: *Homo sapiens* dihydrofolate reductase-thymidylate synthase.

Pharmacophore-based virtual screening

The virtual screening with pharmacophore model No. 10 identified 84.522 and 150 compounds from a catalog of chemical compounds from Sigma-Aldrich® hosted in the Zinc database,[37] and MMV,[38] databases, respectively, with QFIT ranging from 0.28 to 88.77. Next, a cut-off point (equation 2) was applied to narrow the selection, leading to 359 prioritized compounds with QFIT > 71.91. Notably, the remaining molecules after the cut-off point exhibit QFIT values equal to or higher than those of the inhibitors used for model validation. Of these compounds, 105 were discarded as they display recognition requirements similar to human enzymes. Hence, 254 molecules were identified with stereo-electronic requirements for selective interaction with *Lc*DHFR-TS.

It is essential to acknowledge that the previous steps did not focus on minimizing the likelihood of encountering pharmacokinetic issues or ensuring safety for human use. Therefore, additional filters were applied to eliminate potentially problematic molecules concerning these aspects.

Physical-chemical, toxicological filter and commercial availability

The strategies to identify toxicological and physicochemical properties in parallel with predicting intermolecular binding patterns can help avoid prioritizing compounds with potential oral bioavailability and safety issues, reducing costs for subsequent stages in drug development.[75]

The ProTox 3.0[40] and pkCSM[41] toxicity predictive tools were employed in combination to identify, among the compounds selected so far, those without high-risk alerts for acute toxicity (LD_{50}), cardiotoxicity, mutagenic potential (Ames test), hepatotoxicity or carcinogenic potential.

Prediction of toxic potency, particularly the lethal dose in rats (LD_{50}), is a critical starting point for assessing the viability of new drug candidates. ProTox 3.0[40] and pkCSM[41] provide LD_{50} predictions based on datasets containing respectively more than 38,000 and 10,000 compounds structures and LD_{50} data used for model calibration and validation. Cardiotoxicity is another crucial concern in drug design, especially considering the risk of prototype compounds inducing fatal arrhythmias. In this concern, pkCSM[41] places particular emphasis on identifying inhibitors of potassium channels encoded by the hERG (human ether-a-go-go-related gene), as this is the primary molecular target associated with QT prolongation syndrome (a heart rhythm disorder marked by delayed ventricular repolarization, increasing risk of arrhythmias) induced by xenobiotics. ProTox 3.0[41] incorporates a dataset of 1,600 compounds with confirmed cardiotoxicity to calibrate its predictive model for this endpoint.

Mutagenic potential is another key parameter in early-stage drug development decision-making. Accordingly, pkCSM[41] employs a predictive model calibrated with Ames test data from over 8,000 compounds, while ProTox 3.0[40] utilizes mutagenicity data from more than 6,000 substances to develop and validate its model. Additionally, ProTox 3.0[40] includes a carcinogenicity prediction model based on information from 1,390 compounds. An adequate hepatotoxicity profile is also crucial for selecting compounds for further biological evaluation, as hepatotoxicity remains one of the main barriers to successful drug development. The pkCSM[41] model was trained using a dataset of 531 compounds, whereas the ProTox 3.0[40] hepatotoxicity model was constructed based on a training set of 850 compounds.

Considering the construction robustness of both platforms to predict toxicological properties, the selected compounds without toxicity-related alerts to critical endpoints present a strong indication of their favorable safety profile and continuation to subsequent stages of this study.

The Aggregator Advisor was also used to exclude potentially promiscuous compounds (non-specific aggregation).[42,50] Furthermore, oral bioavailability was evaluated using the SwissADME server.[37-39] By integrating these assessments with a commercial availability evaluation of the compounds, 24 molecules without penalties were identified (Table 3).

However, this strategy did not allow the identification of compounds with lower steric interaction penalties against *Lc*DHFR-TS. Thus, the molecular docking technique was employed to predict the binding mode of the best-ranked compounds in the catalytic site of the target.

Docking-based virtual screening to *Lc*DHFR-TS

Construction and evaluation of the *Lc*DHFR-TS model

Molecular docking is a valuable tool for predicting potential interactions and steric penalties between test compounds and target macromolecules, allowing the estimation of ligand-protein affinity.[51] However, due to the unavailability of a high-resolution 3D structure of *Lc*DHFR-TS, for example, in the Protein Data Bank, a 3D structure model of *Lc*DHFR-TS was constructed using homology modeling.

The primary sequence of *Lc*DHFR-TS shares, respectively, 67.3 and 48.0% sequence identity with DHFR-TS from *T. cruzi* and *T. brucei*, indicating a homologous relationship.[76] To construct the homology model, the MODELLER 9.18 program,[44] was first used for multiple sequence alignment (MSA) of the primary sequence of *Lc*DHFR-TS with the 3D structures of *Tc*DHFR-TS (PDB: 3KJS) and *Tb*DHFR (PDB: 3QFX) to reproduce the three-dimensional folding of evolutionarily conserved regions. The MSA method can indicate the global similarity between the sequences,[44] which allowed the generation of a three-dimensional structure model of *L. chagasi* DHFR-TS (Figure S2, Supplementary Information section).

To validate the quality of the structure before performing molecular docking calculations, the model underwent QMEAN score analysis. QMEAN values close to zero indicate good agreement between the structure and the templates of the model, while low-quality models typically score –4.0 or lower.[45] Our selected model obtained a QMEAN score of –0.79, indicating minimal global and local errors compared to the template structures (PDB 3KJS and 3QFX).

For steric evaluation of the model and identification of energetically favorable and unfavorable regions, the modeled structure was analyzed using the Ramachandran

Table 3. Physicochemical properties obtained using the web tool SwissADME[37] for predicting the pharmacokinetic characteristics of potential *Lc*DHFR-TS inhibitors identified in this study

Molecule ID	Molecular mass / Da	TPSA / Å^2	HBD	HBA	cLoP
SUB1	126.12	97.79	3	2	–0.85
SUB2	191.53	112.06	2	6	0.09
SUB3	263.38	44.37	2	2	2.75
SUB4	270.28	78.43	3	4	1.96
SUB5	270.28	78.43	3	3	1.99
SUB6	320.29	82.26	4	4	2.48
SUB7	353.20	82.26	4	2	2.98
SUB8	234.34	41.13	2	1	2.87
SUB9	354.68	132.77	2	6	1.76
SUB10	249.31	70.23	3	2	2.02
SUB11	236.27	82.26	4	2	0.99
SUB12	340.16	90.46	4	3	2.98
SUB13	340.16	90.46	4	3	2.94
SUB14	373.71	90.46	4	6	3.45
SUB15	295.16	41.13	2	1	3.81
SUB16	205.04	55.12	2	1	2.02
SUB17	280.71	63.50	2	3	2.22
SUB18	319.74	90.46	4	3	2.50
SUB19	339.80	109.67	3	4	2.04
SUB20	291.73	63.25	2	3	2.23
SUB21	276.72	61.36	3	2	2.87
SUB22	239.49	55.12	2	1	2.42
SUB23	268.74	47.61	2	3	1.42
SUB24	288.32	122.46	3	4	1.63

*Lc*DHFR-TS: *Leishmania chagasi* dihydrofolate reductase-thymidylate synthase; TPSA: TPSA: topological polar surface area; HBD: hydrogen bond donor count; HBA: hydrogen bond acceptor count; cLoP: octanol water partition coefficient.

plot.[48] The analysis revealed that 96.1% of residues are located in energy-favored regions (Figure S3, Supplementary Information section), demonstrating the stereochemical adequacy of the model.

To further assess the quality of the model, the VERIFY 3D program[47] was applied to determine whether each position of the residues agreed with its expected occurrence. Residues outside the preferred location receive negative values of the 3D-1D score, while score values above 0.20 indicate favorably disposed residues with correct folding according to the graphical analysis[77] (Figure S4, Supplementary Information section). The constructed models showed that 89.62% of *Lc*DHFR-TS residues are present in values above 0.20, suggesting folding compatible with its primary sequence. To compare with templates, 96.47% of *Tc*DHFR-TS (PDB: 3KJS) and 100% of *Tc*DHFR-TS (PDB: 3QFX) have a 3D-1D score above 0.20. All these results indicate that the model has acceptable stereochemical quality and compatible folding, supporting its use for the subsequent step of molecular docking.

Evaluation of molecular docking search parameters

Before conducting the molecular docking analyses against the built model of *Lc*DHFR-TS for the compounds derived from pharmacophoric models screening, the performance of the GOLD 5.3 software,[48] was evaluated.

GOLD 5.3[48] demonstrated that most functions tested achieved RMSD values between the biological and docking-derived poses smaller than 2.0 Å (Figure S5, Supplementary Information section).[78] Among the GOLD 5.3,[48] functions that present adequate RMSD values, the ASP configuration in rescore by Goldscore showed the best discrimination metrics between active compounds and false positives (AUC > 0.9 and enrichment rate of 20%). Consequently, it was selected to perform the screening of compounds obtained from the pharmacophore model screening (Figure 3).[33]

Virtual screening through molecular docking

Based on the parameters defined in the previous step, the score of the 24 selected compounds from Ligand Based Virtual Screening (LBVS) was calculated using the ASP/Goldscore function implemented in the GOLD 5.3 program[48] (Table S2, Supplementary Information section).

The prioritized molecules through molecular docking generally exhibit aromatic structures, lower molecular mass, and contain polar chemical groups capable of acting as hydrogen acceptors/donors. The molecules are also able to participate in hydrophobic and halogen interactions. These characteristics are also observed in known DHFR inhibitors (for example, methotrexate, pyrimethamine, trimethoprim, and trimetrexate).[20-26]

Characterization of the interactions of the prioritized compounds in the virtual screening with the *Lc*DHFR-TS

The interaction profiles of SUB10 and SUB22 compounds, which showed higher predictive affinity against LcDHFR-TS according to docking, share common interactions, including hydrogen bonds with ASP-42 and THR-180, as well as hydrophobic interactions with the residue ILE-45 (Figure 4).

The comparison of the interaction profiles of SUB10 and SUB22 with known DHFR inhibitors, such as methotrexate,[25] reveals that all of them share polar interactions of type hydrogen bonds with Asp-52 and Thr-180, as well as hydrophobic with Phe-56. These findings support the idea that the pharmacophoric search and docking strategies successfully identified ligands with similar interaction patterns to recognized inhibitors of the target.

However, the data obtained from molecular docking notably do not account for the flexibility and potential conformational adjustments imposed on *Lc*DHFR-TS upon ligand binding. To overcome this gap, the complexes formed by SUB10 and SUB22 ligands with *Lc*DHFR-TS

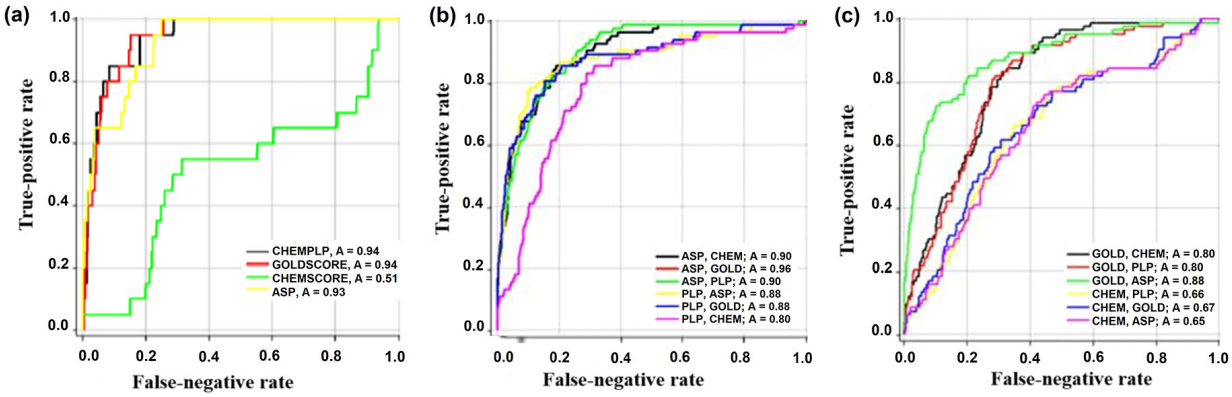

Figure 3. Receiver Operating Character (ROC) curve of discrimination between dihydrofolate reductase (DHFR) inhibitors and decoys by the scoring functions of the GOLD 5.3 program directly (a) and in rescore mode, (b) and (c).

were submitted to molecular dynamics (DM) simulations to validate the interactions obtained from the molecular docking studies.

Molecular dynamic studies

Molecular dynamics is a computational strategy capable of simulating the behavior of molecular systems with complete conformational freedom, providing a robust analysis of stability and details of the interaction between the ligand (e.g., SUB10 and SUB22) with *Lc*DHFR-TS.[79,80]

The initial aspect observed is the geometric stability of the simulated systems over time, for which the root-mean-square deviation of atomic positions (RMSD) analysis of Ca atoms of complexes is classically used. The graph (Figure 5a) shows that the geometries of all simulated systems reach a balance between 60-110 ns of simulation, representing the productive phase of the MD for data extraction.

The *Lc*DHFR-TS apo showed an RMSD range close to 1.0 nm, higher than all other systems, possibly due to the occlusion of the binding sites. Comparatively, the *Lc*DHFR-TS: SUB22, *Lc*DHFR-TS: DHF, *Lc*DHFR-TS: NADPH, and *Lc*DHFR-TS: PYR systems remained within an RMSD range of approximately 0.5 nm, indicating that the presence of ligands promotes a stabilizing effect on the geometry (Figure 5a).

An important complement to the RMSD analysis for assessing the stability of the simulated systems is their degree of compaction or radius of gyration (Rg). This parameter helps identify any tendencies of system disruption along the course of molecular dynamics. The radius of gyration of the simulated systems showed consistent with a range between 2.54 and 2.68 nm throughout the productive phase (60-110 ns) of the MD (Figure 5a), indicating that the *Lc*DHFR-TS maintained its stable 3D structure in an isotonic solution.[81]

The *Lc*DHFR-TS: SUB10 system demonstrates a slight geometric expansion (Rg SUB10 = 2.64 ± 0.02 nm), standing out from the other complexes and corroborating the RMSD data (Rg apo = 2.58 ± 0.01 nm; Rg NADPH = 2.61 ± 0.02 nm; Rg DHF = 2.60 ± 0.01 nm; Rg PYR = 2.62 ± 0.01 nm; and Rg SUB22 = 2.59 ± 0.01 nm) (Figure 5b). To further analyze the residues that most contribute to the geometric variation in each complex, root mean square fluctuation (RMSF) data were obtained from the MD trajectory. These demonstrated that, for the *Lc*DHFR-TS: SUB10 complex, residues between 507 and 512 showed significant fluctuations compared to all other simulated systems (Table S3, Supplementary Information section).

However, as residues 507-512 belong to the TS domain, the combined analysis of RMSD, Rg, and RMSF data suggests that the SUB10 compound influences the movement and accommodation of the *Lc*DHFR-TS structure, particularly in the TS domain. Remarkably, similar fluctuations in the RMSF are not observed for the residues of the DFHR catalytic site compared to the simulated complexes (Figure S5, Supplementary Information section).

To complement the structural stability analyses, the DSSP algorithm (Dictionary of Secondary Structure of Proteins), included in the do_dssp module of GROMACS 2021.3 software,[52-57] was used to evaluate the most likely secondary structures assumed by amino acids from the *Lc*DHFR-TS coordinates in each system throughout the simulations. According to this analysis, the region of catalytic residues 52 to 57 of the *Lc*DHFR-TS: SUB22, *Lc*DHFR-TS: DHF, and *Lc*DHFR-TS: PYR complexes predominantly exhibit an alpha helix organization. However, a turn pattern occurs in the *Lc*DHFR-TS: SUB10 system, especially in the region ASP-52 (Figure S6, Supplementary Information section). As both ASP-52 and 57 are part of an alpha helix formed by amino acids 50 to

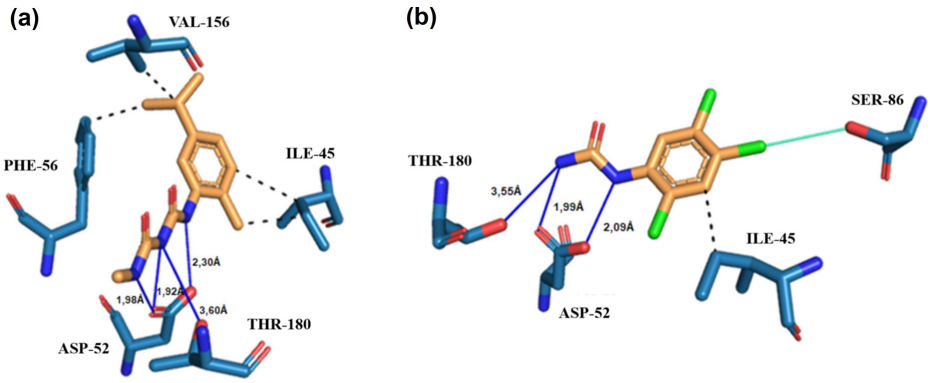

Figure 4. Interaction profiles of SUB10 (a) and SUB22 (b) against *L. chagasi* dihydrofolate reductase thymidylate synthase (*Lc*DHFR-TS) according to molecular docking. The structures are in the stick format: carbons are light blue, nitrogens are dark blue, and oxygens are red. Ligand: carbons are orange, nitrogens are dark blue, and oxygens are red. Interactions: hydrogen interactions are in dark blue straight lines, and hydrophobic interactions are in black dashed lines.

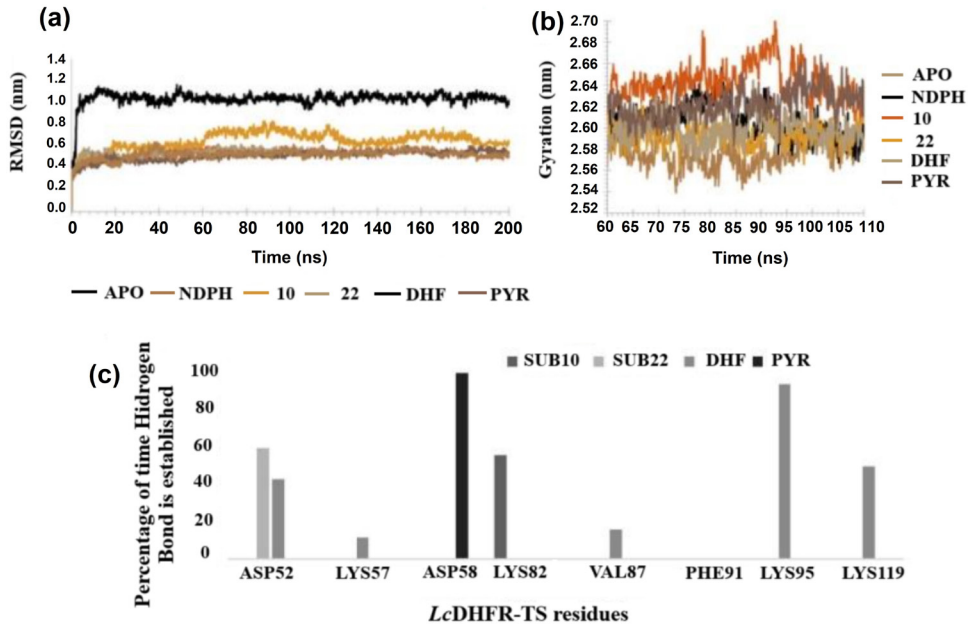

Figure 5. Structural data of simulated systems through MD. (a) Mean square deviation (RMSD) of protein atoms, except hydrogen, during the 200 ns MD of *Lc*DHFR-TS using GROMACS-2021.3. The productive phase period used for data acquisition comprised 60 to 110 ns (RMSD apo = 1.03 ± 0.03 nm; RMSD NADPH = 0.56 ± 0.02 nm; RMSD DHF = 0.52 ± 0.02 nm RMSD PYR = 0.53 ± 0.02 nm, RMSD SUB10 = 0.73 ± 0.04 nm and RMSD SUB22 = 0.56 ± 0.02 nm). (b) Total radius of gyration (Rg) during the productive phase (60-110 ns) of the DM of the *Lc*DHFR-TS complexes (apo, *Lc*DHFR-TS: SUB10, *Lc*DHFR-TS: SUB22, *Lc*DHFR-TS: DHF, *Lc*DHFR-TS: NADPH and *Lc*DHFR-TS: PYR) using the GROMACS-2021.3. (c) Profile of hydrogen bonds between each ligand and *Lc*DHFR-TS in simulated systems during the productive phase.

60, these data suggest that the interaction pattern between SUB10 and *Lc*DHFR-TS differs from the other ligands, mainly in the region affecting the alpha-helix organization.

To gain further insights into the interaction of ASP-52 and the other residues with SUB10 and SUB22, the surface area of interaction between the ligands and *Lc*FHFR-TS was calculated. Among the simulated ligands, the SUB22 compound exhibited the highest surface area of interaction with ASP-52 (24 Å^2), compared to 13 Å^2 for the SUB10 and 11 Å^2 for the DHF (Table S4, Supplementary Information section). On the other hand, for the SUB10 compound, the contact surface data revealed its closer proximity to the Lys-82 residue (31.18 Å^2). This significant interaction is explained by the frequency of hydrogen bonds extracted from the MD trajectory (Figure 5c), which demonstrates that such interactions occur with the Lys-82 residue 56% of the time in the productive phase, underscoring the importance of Lys-82 for the interaction between SUB10 compound and *Lc*DHFR-TS.

The contact surface analysis also highlights several prominent residues in the interactions. For the compound SUB10, Ile-45 (31.70 Å^2) and Tyr-83 (20.99 Å^2) are noteworthy, while for the SUB22 compound, Ile-45 (26.73 Å^2), Met-53 (30.42 Å^2), Phe-56 (22 .43 Å^2), Thr-83 (25.41 Å^2), and Val-156 (26.01 Å^2) stand out (Table S4).

While the structural information is essential for understanding the interactions of SUB10 and SUB22 with *Lc*DHFR-TS, it does not shed light on the effect on the system's free energy. Thus, the Molecular Mechanics/Poisson-Boltzmann Surface Area (MM/PBSA)[80] was employed to determine each residue's contribution to the free energy of the system. The MM/PBSA[80] analysis revealed that the interaction of the Lys-82 residue with the SUB10 compound energetically contributes to the stabilization of the system by –0.4 kJ mol^{-1} (Figure 6), corroborating the data on hydrogen bonding and contact surface. Additionally, the MM/PBSA[80] analysis demonstrated an outstanding contribution (–5.18 kJ mol^{-1}) for the stabilization of the system through the interaction of Ile-45 with SUB10, further supporting the data of the expressive contact surface between Ile-45 and SUB10.

For compound SUB22, the residues Met-53, Phe-56, and Val-156 also contribute to the stabilization of the complex by –0.18, –0.40, and –0.25 kJ mol^{-1}, respectively. These energetic patterns for these residues align with the contact surface data, indicating their significant role in the interaction between this compound and *Lc*DHFR-TS.

Finally, the MM/PBSA data demonstrated that the presence of the SUB10 compound had a greater capacity to stabilize the system compared to the SUB22 compound, with free energy variations estimated at –3.59 ± 0.36 and –0.51 ± 0.25 kJ mol^{-1}, respectively. While these ΔG values (free energy change, indicating the spontaneity and favorability of a molecular interaction) may seem less

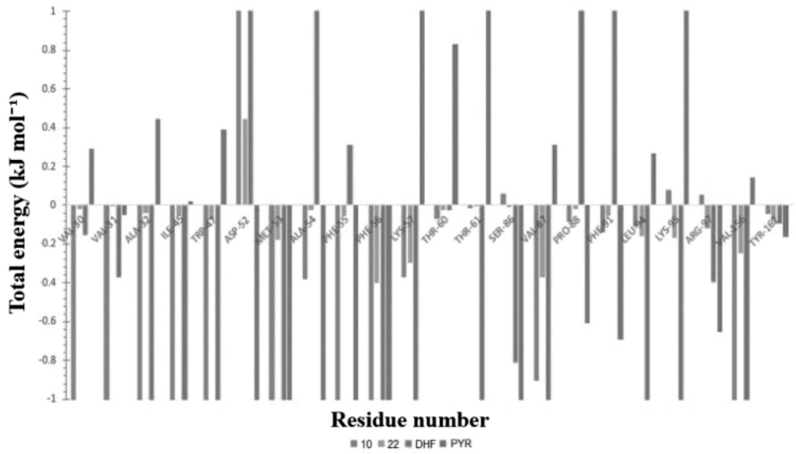

Figure 6. Free energy of binding of compounds calculated using Molecular Mechanics/Poisson-Boltzmann Surface Area (MM/PBSA).[80]

favorable when compared to PYR (–8.5 ± 0.15 kJ mol^{-1}), a known competitive DHFR inhibitor, the binding efficiency measure for SUB10 and SUB22 compounds (–0.20 and –0.04 kJ atom^{-1} mol^{-1}, respectively) revealed that SUB10, in particular, is very close to the value of 0.29 kJ atom^{-1} mol^{-1} suggested by Hopkins *et al*.[82] for ligands with excellent potential for optimization.

Although the *in silico* approaches employed in this study are valuable and widely used tools in drug discovery and early-stage candidate screening, it is essential to acknowledge their inherent limitations. These computational methods provide predictions based on theoretical models which, despite being robust and well-calibrated, cannot fully replicate the complexity of biological systems. The results reflect theoretical binding affinity and conformational stability of the compounds with the target enzyme but do not guarantee biological efficacy or the absence of toxicity in cellular systems or living organisms.

Key factors such as bioavailability, metabolism, off-target effects, and physiological responses are not fully captured by these computational tools. Therefore, despite the promising profiles demonstrated by compounds SUB10 and SUB22 in terms of selectivity and predictive pharmacokinetic and toxicological properties, the absence of experimental validation, whether *in vitro* or *in vivo*, limits definitive conclusions regarding their actual efficacy and safety. Consequently, the data presented should be interpreted as a preliminary step in the drug discovery process, underscoring the need for subsequent experimental studies to confirm these findings and support further development within the drug discovery pipeline.

Conclusions

Using pharmacophore and docking-based virtual screening approaches represents a promising strategy for identifying compounds with potential pharmacological relevance against targets from neglected diseases, such as *L. chagasi*, the etiological agent of visceral leishmaniasis.

In the present work, virtual screening through pharmacophoric models, physicochemical, and toxicological filters applied to an extensive database (comprising 214,446 substances) successfully identified compounds possessing the stereo-electronic requirements to bind to *Lc*DHFR-TS. Models 10 of *Lc*DHFR-TS and 3 of *Hs*DHFR, built using the GALAHADTM module, demonstrated sufficient sensitivity and specificity for screening potential selective inhibitors against *Lc*DHFR-TS.

Furthermore, the homology modeling approach proved valuable for providing a 3D structure of *Lc*DHFR-TS that is useful for molecular docking studies in the virtual screening process. Molecular docking assays in the structure of *Lc*DHFR-TS showed sensitivity and specificity in identifying active compounds during the validation step, employing the ASP function in rescore by Goldscore within the GOLD 5.3 software.

The subsequent analyses based on molecular dynamics simulation demonstrated that the ligands SUB10 and SUB22 could effectively bind to the catalytic site of *Lc*DHFR-TS, promoting system stabilization. The data indicate that SUB10 and SUB22 carry out hydrogen interactions with the LYS-82 and ASP-52 residues, respectively, keeping for more than 50% of the simulation time, indicating the potential occurrence of such interaction patterns in a biological environment.

Finally, the MM/PBSA analyses confirmed the contribution of both SUB10 and SUB22 to the complex stabilization, with SUB10 displaying a relatively more significant contribution. Moreover, the measurement of binding efficiency for compounds SUB10 and SUB22 (–0.20 and –0.04 kJ atom^{-1} mol^{-1}, respectively) demonstrated that SUB10 has particular potential for lead optimization.

Supplementary Information

Supplementary data are available free of charge at http://jbcs.sbq.org.br as PDF file.

Data Availability Statement

All data generated or analyzed during this study are included in the main text of the article.

Acknowledgments

The authors thank CENAPAD-SP (National Center for High-Performance Computing in São Paulo) and UNICAMP/FINEP - MCT (project IDs: proj651 and proj822). This work was supported by the Brazilian National Council for Scientific and Technological Development (CNPq), Brazilian Coordination for Improvement of Personnel Higher Education (CAPES) and Bahia Research Foundation (FAPESB, grant numbers APP071/2011, JCB-0039/2013 and RED-008/2013, respectively). We also thank Mr Michael Rosenberg (Florida-USA) for the English grammar revisions of this manuscript.

Author Contributions

Luíza M. de Macêdo was responsible for investigation, writing original draft; Quezia V. F. S. da Fonseca for investigation; Iris C. dos Santos for investigation; Quézia L. S. Sampaio for investigation; Janine F. S. Silva for writing (review and editing); Moyses F. de Araujo Neto for investigation, writing (review and editing); Franco Henrique A. Leite for resources; Samuel S. R. Pita for resources, formal analysis, methodology, validation and visualization; Erika Maria O. Ribeiro writing (review and editing); Aníbal F. Santos Júnior for resources; André L. B. Teles for conceptualization, methodology, formal analysis, writing original draft, supervision.

References

1. World Health Organization (WHO); *Global Leishmaniasis Surveillance: 2019-2020, A Baseline for the 2030 Roadmap - Weekly Epidemiological Record*; WHO: Switzerland, 2021. [Link] accessed in June 2025
2. Agência Fiocruz de Notícias; *Doenças Negligenciadas*; Fiocruz: Rio de Janeiro, 2013. [Link] accessed in June 2025
3. Martins, I. M. L.; Silva, J. S.; Campos, D. K. O.; Oliveira, R. S.; Silva, P. L. N.; Carvalho, S. F. G.; Caldeira, A. P. *J.*; *Bras. Patol. Med. Lab.* **2021**, *57*, e2702021. [Crossref]
4. Brindha, J.; Balamurali, M. M.; Kaushik Chanda; *Front. Chem.* **2021**, *12*, 622286. [Crossref]
5. Batista, F. M. A.; Souza, R. A.; Aguiar, B. G. A.; Ibiapina, A. B. L.; Albuquerque, P. A.; Mendonça, V. J.; Costa, C. H. N.; *Cad. Saúde Pública* **2021**, *37*, e00340320. [Crossref]
6. Ferreira, J. R. S.; Silva, K. M.; Almeida, M. S. G.; Gomes, D. C. S.; Cavalcanti, M. G. S.; Ferreira-Júnior, G. C.; Alves, L. C.; Brayner, F. A.; Matos-Rocha, T. J.; *Braz. J. Biol.* **2022**, *82*, e238383. [Crossref]
7. Organização Pan-Americana da Saúde (OPAS); *Leishmanioses, Informe Epidemiológico das Américas*, OPAS: Washington, D.C., 2021. [Link] accessed in June 2025
8. Organização Pan-Americana da Saúde (OPAS); *Leishmanioses, Informe Epidemiológico das Américas*; OPAS: Washington, D.C., 2019. [Link] accessed in June 2025
9. Ministério da Saúde, Secretaria de Vigilância em Saúde (MS-SVS); *Manual de Vigilância da Leishmaniose Tegumentar*, 2nd ed.; Ministério da Saúde: Brasília, Brazil, 2017. [Crossref]
10. de Moraes, A. R. D. P.; Tavares, G. D.; Rocha, F. J. S.; Paula, E.; Giorgio, S.; *Exp. Parasitol.* **2018**, *187*, 12. [Crossref]
11. Brum, N. F. F.; Coelho, J. S.; Carvalho, L. S.; Vieira, M. N. O.; Bentes, A. A.; Carellos, E. V. M.; Diniz, L. M. O.; Carvalho, A. L.; Romanelli, R. M. C.; *Rev. Paul. Pediatr.* **2022**, *40*, e2020269. [Crossref]
12. Bezerra-Souza, A.; Yanamoto, E. S.; Laurenti, M. D.; Ribeiro, S. P.; Passero, L. F.; *Parasitol. Int.* **2016**, *65*, 702. [Crossref]
13. Da Silva, B. J. M.; Hage, A. A. P.; Silva, E. O.; Rodrigues, A. P. D.; *J. Integr. Med.* **2018**, *16*, 211. [Crossref]
14. Raimondi, M. V.; Randazzo, O.; La Franca, M.; Barone, G.; Vianoni, E.; Rossi, D.; Collina, S.; *Molecules* **2019**, *24*, 1140. [Crossref]
15. Martins, J. P. M.: *Triagem Virtual de Inibidores da Enzima Di-hidrofolato Redutase de Schistosoma mansoni (SmDHFR)*; MSc Dissertation, Universidade de São Paulo, 2017. [Link] accessed in June 2025
16. Zuccotto, F.; Martin, A. C.; Laskowski, R.A.; Thornton, J. M.; Gilbert, I. H.; *J. Comput. Aided Mol. Des.* **1998**, *12*, 241. [Crossref]
17. Matos, I. A.: *Planejamento in silico de Inibidores da Enzima Dihidrofolato Redutase*; MSc Dissertation, Universidade Federal de Sergipe, Sergipe, Brazil, 2016. [Link] accessed in June 2025
18. Vickers, T. J.; Beverley, S.; *Essays Biochem.* **2011**, *51*, 51. [Crossref]
19. Schell, J. R.; Dyson, H. J.; Wright, P. E.; *Annu. Rev. Biophys. Biomol. Struct.* **2004**, *33*, 119. [Crossref]
20. Teixeira, B. V. F.; Teles, A. L. B.; Silva, S. G. D.; Brito, C. C. B.; Freitas, H. F.; Pires, A. B. L.; Froes, T. Q.; Castilho, M. S.; *J. Enzyme Inhib. Med. Chem.* **2019**, *34*, 1439. [Crossref] [PubMed]
21. Hardy, L. W.; Matthews, W.; Nare, B.; Beverley, S. M.; *Exp. Parasitol.* **1997**, *87*, 157. [Crossref]
22. Gilbert, I. H.; *Biochim. Biophys. Acta* **2002**, *1587*, 249. [Crossref][PubMed]
23. Pez, D.; Leal, I.; Zuccotto, F.; Boussard, C.; Brun, R.; Croft, S. L.; Yardley, V.; Ruiz Perez, L. M.; Gonzalez Pacanowska, D.;

Gilbert, I. H.; *Bioorg. Med. Chem.* **2003**, *11*, 4693. [Crossref] [PubMed]
24. Khabnadideh, S.; Pez, D.; Musso, A.; Brun, R.; Pérez, L. M.; González-Pacanowska, D.; Gilbert, I. H.; *Bioorg. Med. Chem.* **2005**, *13*, 2637. [Crossref] [PubMed]
25. Gangjee, A.; Kurup, S.; Namjoshi, O.; *Curr. Pharm. Des.* **2007**, *13*, 609. [Crossref] [PubMed]
26. Sharma, V. K.; Bharatam, P. V.; *J. Comput. Biol.* **2020**, *27*, 43. [Crossref] [PubMed]
27. Karabulut, S.; Sizochenko, N.; Orhan, A.; Leszczynski, J.; *J. Mol. Graph. Model.* **2016**, *70*, 23. [Crossref] [PubMed]
28. Mysinger, M. M.; Carchia, M.; Irwin, J. J.; Shoichet, B. K.; *J. Med. Chem.* **2012**, *55*, 6582. [Crossref] [PubMed]
29. *Marvin Sketch*®, version 15.4.20, ChemAxon, 2015.
30. *Sybyl*®-*X* 2.0, version 2.0; Tripos, St Louis, MO, USA, 2010.
31. Clark, M.; Cramer III, R. D.; Van Opdenbosch, N.; *J. Comp. Chem.* **1989**, *10*, 982. [Crossref]
32. Gasteiger, J.; Marsili, M.; *Tetrahedron* **1980**, *36*, 3219. [Crossref]
33. Gigliarano, C.; Figini, S.; Muliere, P.; *Comput. Stat. Data Anal.* **2014**, *77*, 300. [Crossref]
34. Lätti, S.; Niinivehmas, S.; Pentikäinen, O. T.; *J. Cheminform.* **2016**, *8*, 45. [Crossref]
35. Sterling, T.; Irwin, J. J.; *J. Chem. Inf. Model.* **2015**, *55*, 2324. [Crossref][PubMed]
36. Medicines for Malaria Venture; https://www.mmv.org/, accessed in June 2025.
37. Daina, A.; Michielin, O.; Zoete, V.; *Sci. Rep.* **2017**, *7*, 42717. [Crossref][PubMed]
38. Lipinski, C. A.; Lombardo, F.; Dominy, B. W.; Feeney, P. J.; *Adv. Drug Delivery Rev.* **2001**, *46*, 3. [Crossref]
39. Veber, D. F.; Johnson, S. R.; Cheng, H. Y.; Smith, B. R.; Ward, K. W.; Kopple, K. D.; *J. Med. Chem.* **2002**, *45*, 2615. [Crossref] [PubMed]
40. Banerjee, P.; Kemmler, E.; Dunkel, M.; Preissner, R.; *Nucleic Acids Res.* **2024**, *52*, W513. [Crossref]
41. Pires, D. E. V.; Blundell, T. L.; Ascher, D. B.; *J. Med. Chem.* **2015**, *58*, 4066. [Crossref][PubMed]
42. Irwin, J. J.; Duan, D.; Torosyan, H.; Doak, A. K.; Ziebart, K. T.; Sterling, T.; Tumanian, G.; Shoichet, B. K.; *J. Med. Chem.* **2015**, *58*, 7076. [Crossref][PubMed]
43. Sievers, F.; Wilm, A.; Dineen, D.; Gibson, T. J.; Karplus, W.; Li, R.; Lopez, R.; McWilliam, H.; Remmert, M.; Söding, J.; Thompson, J. D.; Higgins, D. G.; *Mol. Syst. Biol.* **2011**, *7*, 539. [Crossref][PubMed]
44. Šali, A.; Webb, B.; Madhusudhan, M. S.; Shen, M.; Dong, D.; Martı-Renom, M. A.; Eswar, N.; Alber, F.; Topf, M.; Oliva, B.; Fiser, A.; Sánchez, R.; Yerkovich, B.; *MODELLER A Program for Protein Structure Modeling Release* v. 9.18; University of California San Francisco, San Francisco, CA 94143, USA, 2017.
45. Benkert, P.; Tosatto, S. C. E.; Schomburg, D.; *Proteins* **2008**, *71*, 261. [Crossref][PubMed]
46. Colovos, C.; Yeates, T. O.; *Protein Sci.* **1993**, *2*, 1511. [Crossref] [PubMed]
47. Eisenberg, D.; Luthy, R.; Bowie, J. U.; *Methods Enzymol.* **1997**, *277*, 396. [Crossref][PubMed]
48. Jones, G.; Willett, P.; Glen, R. C.; Leach, A. R.; Taylor, R. J.; *Mol. Biol.* **1997**, *267*, 727. [Crossref]
49. Anandakrishnan, R.; Aguilar, B.; Onufriev, A. V.; *Nucleic Acids Res.* **2012**, *40*, W537. [Crossref]
50. Sinatti, V. V. C.; Baptista, L. P. R.; Alves-Ferreira, M.; Dardenne, L.; da Silva, J. H. M.; Guimarães, A. C.; *J. Mol. Graph. Model.* **2017**, *77*, 168. [Crossref]
51. Leite, F. H. A.: *Planejamento e Avaliação de Novos Inibidores de Pteridina Reductase 1 (PTR1) de Leishmania major*; PhD Thesis, Universidade Estadual de Feira de Santana, Feira de Santana, Brazil, 2015. [Link] accessed in June 2025
52. van der Spoel, D.; Lindahl, E.; Hess, B.; Groenhof, G.; Mark, A. E.; *J. Comput. Chem.* **2005**, *26*, 1701. [Crossref] [PubMed]
53. Bekker, H.; Berendsen, H. J. C.; Dijkstra, E. J.; Achterop, S.; van Drunen, R.; van der Spoel, D.; Sijbers, A.; Keegstra, H.; *Phys. Comp.* **1993**, *92*, 252. [Crossref]
54. Berendsen, H. J. C.; van der Spoel, D.; van Drunen, R.; *Comp. Phys. Comm.* **1995**, *91*, 43. [Crossref]
55. Lindahl, E.; Hess, B.; van der Spoel, D.; *J. Mol. Mod.* **2001**, *7*, 306. [Crossref]
56. Hess, B.; Kutzner, C.; van der Spoel, D.; Lindahl, E.; *J. Chem. Theory Comput.* **2008**, *4*, 435. [Crossref][PubMed]
57. Pronk, S.; Páll, S.; Schulz, R.; Larsson, P.; Bjelkmar, P.; Apostolov, R.; Shirts, M. R.; Smith, J. C.; Kasson, P. M.; van der Spoel, D.; Hess, B.; Lindahl, E.; *Bioinformatics* **2013**, *29*, 845. [Crossref][PubMed]
58. Gomes, D. E. B.; da Silva, A. W. S.; Lins, R. D.; Pascutti, P. G.; Soares, T. A.; *HbMap2Grace*; Universidade Federal do Rio de Janeiro, 2016. [Crossref]
59. Gomes, D. E. B.; Limaverde, G. S. C. S.; Wilter, A. S. S.; Pascutti, P. G.; *SurfinMD*, version 1.06p4; Universidade Federal do Rio de Janeiro, 2016. [Crossref]
60. Malde, A.K.; Zuo, L.; Breeze, M.; Stroet, M.; Poger, D.; Nair, P. C.; Oostenbrink, C.; Mark, A. E.; *J. Chem. Theory Comput.* **2011**, *7*, 4026. [Crossref]
61. Vanichtanankul, J.; Taweechai, S.; Yuvaniyama, J.; Vilaivan, T.; Chitnumsub, P.; Kamchonwongpaisan, S.; Yuthavong, Y.; *ACS Chem. Biol.* **2011**, *6*, 905. [Crossref]
62. Schmid, N.; Eichenberger, A. P.; Choutko, A.; Riniker, S.; Winger, M.; Mark, A. E.; van Gunsteren, W. F.; *Eur. Biophys. J.* **2011**, *40*, 843. [Crossref][PubMed]
63. Teles, A. L. B.; Silva, R. R.; Ko, M.; Ferreira, G. M.; Pita, S. D. R.; Trossini, G. H. G.; Carvalho, P.; Castilho, M. S.; *Curr. Top. Med. Chem.* **2018**, *18*, 406. [Crossref]

64. Andrade, C. R. B.: *Caracterização Química das Folhas e Avaliação in sílico dos Metabólitos Isolados de Zanthoxylum caribaeum LAM (Rutaceae)*; PhD Thesis, Universidade Estadual de Feira de Santana, Feira de Santana, Brazil, 2018. [Link] accessed in June 2025
65. Lionta, E.; Spyrou, G.; Vassilatis, D. K.; Cournia, Z.; *Curr. Top. Med. Chem.* **2014**, *14*, 1923. [Crossref][PubMed]
66. Zhao, X.; Yuan, M.; Huang, B.; Ji, H.; Zhu, L.; *J. Mol. Graph. Model.* **2010**, *29*, 126. [Crossref][PubMed]
67. Liu, M.; Wu, Q.; Hu, W.; *Chin. J. Chem.* **2011**, *29*, 1075. [Crossref]
68. Yang, S.-Y.; *Drug Discovery Today* **2010**, *15*, 444. [Crossref]
69. Martinez, E. Z.; Louzada-Neto, F.; Pereira, B. D. B.; *Cad. Saúde Coletiva* **2003**, *11*, 7. [Crossref]
70. Shepphird, J. K.; Clark, R. D.; *J. Comput. Aided. Mol. Des.* **2006**, *20*, 763. [Crossref][PubMed]
71. Kumar, A.; Siddiqi, M. I.; *J. Mol. Graph. Model.* **2008**, *27*, 476. [Crossref][PubMed]
72. Schormann, N.; Senkovich, O.; Walker, K.; Wright, D. L.; Anderson, A. C.; Rosowsky, A.; Ananthan, S.; Shinkre, B.; Velu, S.; Chattopadhyay, D.; *Proteins* **2008**, *73*, 889. [Crossref] [PubMed]
73. Arooj, M.; Sakkiah, S.; Cao, G. P.; Lee, K. W.; *PLoS One* **2013**, *8*, e60470. [Crossref] [PubMed]
74. Rana, R. M.; Rampogu, S.; Zeb, A.; Son, M.; Park, C.; Lee, G.; Yoon, S.; Baek, A.; Parameswaran, S.; Park, S. J.; Lee, K. W.; *J. Clin. Med.* **2019**, *8*, 233. [Crossref] [PubMed]
75. Dickson, M.; Gagnon, J. P.; *Nat. Rev. Drug Discovery* **2004**, *3*, 417. [Crossref] [PubMed]
76. Krissinel, E.; *Bioinformatics* **2007**, *23*, 717. [Crossref]
77. Freitas, H. F.: *Estudo de QSAR 2D para uma Série de Derivados Azólicos Ativos contra Cryptococus e de Mecanismos de Resistência de Cryptococus gattii através de Modelagem por Homologia*; MSc Dissertation, Universidade Federal da Bahia, Bahia, Brazil, 2011. [Link] accessed in June 2025
78. Mizutani, M. Y.; Takamatsu, Y.; Ichinose, T.; Nakamura, K.; Itai, A.; *Proteins* **2006**, *63*, 878. [Crossref] [PubMed]
79. Homeyer, N.; Gohlke, H.; *Mol. Inform.* **2012**, *31*, 114. [Crossref]
80. Leite, F. H. A.; Froes, T. Q.; da Silva, S. G.; de Souza, E. I. M.; Vital-Fujii, D. G.; Trossini, G. H. G.; Pita, S. S. D. R.; Castilho, M. S.; *Eur. J. Med. Chem.* **2017**, *132*, 322. [Crossref]
81. Sneha, P.; Doss, C. G.; *Adv. Protein Chem. Struct. Biol.* **2016**, *102*, 181. [Crossref][PubMed]
82. Hopkins, A. L.; Groom, C. R.; Alex, A.; *Drug Discovery Today* **2004**, *9*, 430. [Crossref]

Submitted: April 7, 2025
Published online: July 3, 2025